RESEARCH ARTICLE `OPEN ACCESS`

Elucidating Parasitic Currents in Proton-Exchange-Membrane Electrolytic Cells via Physics-Based and Data-Driven Modeling

Violeta Karyofylli[1] [iD] | K. Ashoke Raman[1] | Linus Hammacher[1,2] | Yannik Danner[1,2] | Hans Kungl[1] | André Karl[1] | Eva Jodat[1] | Rüdiger-A. Eichel[1,2,3]

[1]Institute of Energy Technologies, Fundamental Electrochemistry (IET-1), Forschungszentrum Jülich GmbH, Jülich, Germany | [2]Institute of Physical Chemistry, RWTH Aachen University, Aachen, Germany | [3]Faculty of Mechanical Engineering, RWTH Aachen University, Aachen, Germany

Correspondence: Violeta Karyofylli (v.karyofylli@fz-juelich.de)

ABSTRACT

Proton-exchange membrane (PEM) water electrolysis is pivotal for green hydrogen production, necessitating accurate predictive models to manage their non-linearities and expedite commercial deployment. Understanding degradation mechanisms through macro-scale modeling and uncertainty quantification (UQ) is crucial for advancing this technology via efficiency enhancement and lifetime extension. This study primarily utilizes a one-dimensional physics-based model to elucidate the presence of electron transport within the PEM, another degradation phenomenon, besides gas crossover. This work also applies a machine learning (ML) algorithm, such as eXtreme Gradient Boosting (XGBoost), to model PEM electrolytic cell (PEMEC) operation based on a dataset generated from the previously mentioned physics-based model. The ML model excels in predicting the polarization behavior. Based on this surrogate model, UQ and sensitivity analysis are finally employed to enlighten the dependence of PEMECs performance and Faradaic efficiency on the effective electronic conductivity of PEM, especially when electronic pathways exist within the membrane and operating at low current densities.

1 | Introduction

Hydrogen production plays a key role in energy transition at national and international levels. European countries are planning to expand electrolysis capacity up to 52 GW by 2030, with the European Union targeting 40 GW by 2030 and Germany aiming for 10 GW by the same year [1–3]. A promising approach for hydrogen production is the use of proton-exchange membrane electrolytic cells (PEMECs) for water electrolysis as they provide fast response time and dynamic operations which are essential for their coupling with intermittently available renewable energy sources [4, 5]. Additional advantages of PEMECs include their

---

Abbreviations: R^2, coefficient of determination; aCL, anodic catalyst layer; aPTL, anodic porous transport layer; AST, acceleration stress test; BC, boundary condition; cCL, cathodic catalyst layer; CL, catalyst layer; cPTL, cathodic porous transport layer; EOD, electro-osmotic drag; HER, hydrogen evolution reaction; HTE, high-throughput experimentation; MEA, membrane-electrode assembly; ML, machine learning; MSE, mean square error; ODE, ordinary differential equation; OER, oxygen evolution reaction; PDF, probability density function; PEM, proton-exchange membrane; PEMEC, PEM electrolytic cell; PEMFC, PEM fuel cell; PI, prediction interval; PTL, porous transport layer; SA, sensitivity analysis; SD, standard deviation; SI, Sobol indices; UQ, uncertainty quantification; XGBoost, eXtreme Gradient Boosting.

- -

possibility for operation at high current densities ($> 2\,Acm^{-2}$) and their compact system design [6–8]. Future development of PEMECs aims to reduce capital expenditure and enhance its long-term stability over 100,000 h [8–11]. Unfortunately, long-term stability is primarily challenged by degradation effects in PEMECs, especially within the membrane-electrode assembly (MEA), which comprises the membrane and catalyst layers. Various failure mechanisms may occur, with catalyst degradation involving dissolution, passivation, agglomeration, or poisoning [12–15]. Membrane degradation mechanisms can be categorized into mechanical, thermal, and chemical degradation [14, 16, 17].

Although studies on PEMEC degradation are fewer compared to PEM fuel cells (PEMFCs), degradation mechanisms and their stressors have been widely discussed and investigated experimentally [10]. A widely observed degradation mechanism is membrane thinning. Radicals like hydrogen peroxide (H_2O_2) can be formed as a result of gas crossover, which attack the ionomer backbone of perfluoroalkyl sulfonic acid membranes (e.g., Nafion) [10, 14, 16]. Experimental studies indicate that gas crossover depends on operating conditions. For example, a strong linear increase in gas crossover has been reported with rising current density [18]. A model-based study further highlights H_2-in-O_2 overshoots in the anode due to instant down steps in current density [19]. Additionally, temperature (60–80°C) also affects the H_2-gas crossover, while the gas crossover is triggered by the acceleration stress test (AST) [16]. Higher temperatures (80°C) led to a higher gas crossover, which indicates a performance loss. Similarly, high temperatures led to increased membrane thinning over time, linked to high gas crossover rates [20]. Radical-induced chemical degradation of the membrane is intensified by the Fenton reaction in the presence of radical-forming metal cations, like Fe^{3+}, as investigated in several studies [16, 21–23].

Mechanical degradation mechanisms in PEMECs include the formation of pinholes or membrane cracking, which can be triggered by local temperature or current hotspots and membrane drying [6, 12, 24, 25]. The impact of membrane pinholes on PEMEC performance has been already examined by conducting efficiency tests on intentionally perforated membranes [26]. Membranes with the largest pinholes exhibited twice the H_2-gas crossover compared to pristine ones. This study underscored the interdependence of various degradation mechanisms and their potential to exacerbate each other. Thin membrane designs, aiming at reducing ionic resistance and improving efficiency, also contribute to increased mechanical instability and gas crossover [6, 10]. Performance tests on three different Nafion membranes (NR212, N115, N117) with thicknesses of 50, 127 and 180 µm. respectively, revealed that the thinnest membrane (Nafion NR212) exhibited the most significant voltage increase after 144 h of operation, attributed to severe degradation due to pinhole formation [27].

A frequently observed but not fully understood degradation effect is the parasitic current due to electron conduction through the membrane, leading to lower Faradaic efficiency. One possible cause of these parasitic currents is mechanical membrane degradation during long-term high-current density operations [7]. Studies have shown that the overall electronic resistance through the plane decreases over time due to increased short circuit paths, resulting in a reduced initial slope on the polarization curve

and voltage drops below the thermo-neutral voltage after several hours of operation at low currents. Mechanical degradation in PEMFC membranes has also been documented, indicating that even pristine membrane samples show some inhomogeneity, initiating micro-crack formation during operation [28]. The active electrode material fills these surface cracks, reducing locally the distance between the anode and cathode and thereby lowering electrical resistance. Over time, these cracks can propagate, ultimately leading to parasitic currents. Membranes still in development and lacking mechanical robustness, such as hydrocarbon ones, can exhibit a higher likelihood of parasitic currents in PEMECs compared to typical Nafion membranes [29]. The polarization curves from long-term operations show a decreased slope for the less mechanically robust membranes. This phenomenon has been attributed to the formation of radicals due to Fe contamination, which leads to parasitic currents over time. A similar effect has been detected in another study on an NR212 membrane [27], where voltage drops below the thermoneutral voltage at low current densities ($0.01\,Acm^{-2}$) were noted. Mechanically induced pinholes and cracks in the membrane can lead to increased gas crossover and parasitic currents [26]. In PEMFCs, electrical short results in an increased slope of the polarization curve [30]. Further experimental investigations on the influence of parasitic currents in dynamic PEMFC experiments have been conducted to assess their feasibility for grid integration [31]. However, mechanical degradation is not the only cause of parasitic currents. In PEMECs, for example, electrically conductive iridium catalyst particles can migrate from the anode across the membrane to the platinum/carbon cathode, a phenomenon known as catalyst dissolution and diffusion [32]. This substitution of protons in the membrane by conductive cations was also observed after operating an MEA for PEMECs fabricated via reactive spray deposition for 5000 h [33]. In a very recent study, cross-plane formation of iridium filaments within the membrane was discovered. This formation is highly correlated to the interface between the anodic porous transport layer (aPTL) and anodic catalyst layer (aCL) [34] and leads to parasitic currents.

Overall, literature studies primarily offer hypotheses for degradation sources [12]. Unfortunately, the complete degradation pathways are not fully understood yet. This is partly due to the limitations of electrochemical experiments and analytical methods [6], which often require ex-situ detection and analysis, intentional triggering via AST, or costly long-term studies [15, 16, 26]. Therefore, model-based investigations can be instrumental in understanding degradation pathways, quantifying their impact on PEMEC performance, and efficiently planning further experiments [4, 35]. As the focus of our paper is on modeling the effects of parasitic currents on PEMECs, we begin with a summary of existing literature approaches. A first attempt to further understand these effects has been already made, having as an outcome a qualitative model of the overall cell behavior in terms of electrical equivalent circuits [7]. Moreover, a one-dimensional (1D) steady-state model has been developed to examine the effect of gas crossover on PEMECs, proposing that parasitic currents can be generated due to H_2 re-oxidation and O_2 reduction, when H_2 and O_2 reach the opposite electrodes [36]. Similarly, a zero-dimensional model has been designed and the computation of Faradaic efficiency accounts for parasitic current effects [37]. In the context of PEMFCs, a different study proposed a 1D five-layer steady-state model incorporating membrane electrical resistance
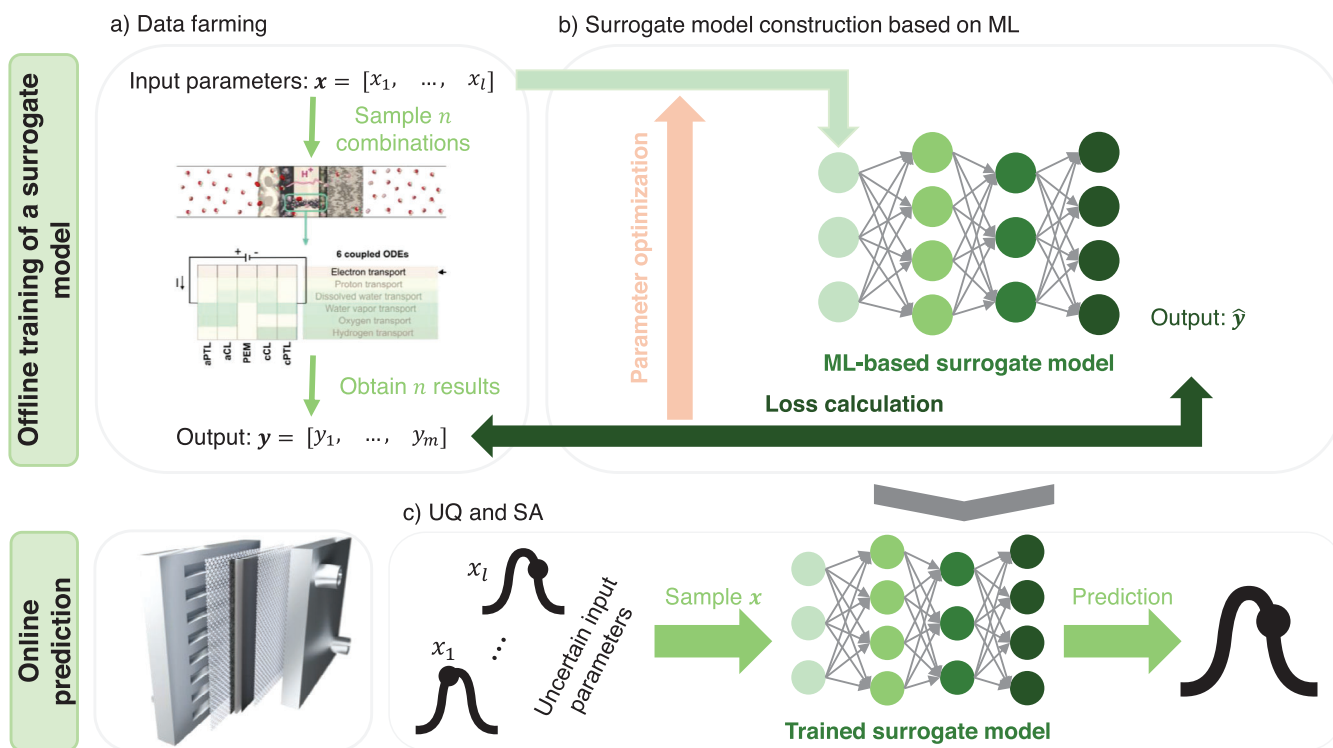
FIGURE 1 | Schematic overview of the proposed UQ and SA framework (adapted from [39]). An ML algorithm, namely XGBoost was trained with datasets generated from 1D physics-based simulations. These datasets were created by randomly sampling eight input parameters and by collecting the corresponding simulation outputs related to the polarization behaviour and Faradaic efficiency of a PEMEC. After acquiring the data and training the model during the offline phase, the surrogate model was employed in the online phase to quickly predict outputs, enabling fast and efficient UQ and SA.

as a function of mechanical contact pressure [38]. This study found that increasing the anodic pressure and decreasing the cathodic one reduces the electrical resistance of the membrane.

In the following sections, we present a 1D steady-state physics-based model for PEMECs, addressing specifically the effect of parasitic currents on Faradaic efficiency and cell performance under varying cell-component parameters. This model neglects other degradation effects such as gas crossover or membrane thinning caused by undesired chemical reactions. A dataset from the aforementioned model is generated and used to train a machine learning (ML) surrogate model. Its performance is analyzed to assess the potential of ML in accurately and quickly predicting the effects of parasitic currents in PEMECs (Figure 1). Section 2 details the mathematical setup of the physics-based model, whereas Section 3 the applied ML concepts. Section 4 explores the impact of parameters such as the effective electronic conductivity within a proton-exchange membrane (PEM) on a PEMEC affected by parasitic currents. These findings are further examined through uncertainty quantification (UQ) and sensitivity analysis (sensitivity analysis (SA)) by means of an ML-based surrogate model, providing a valuable foundation for future investigations into the effects of parasitic currents on PEMECs.

2 | Mathematical Model

From the literature overview above, the first attempt to understand parasitic currents within MEAs was made using electrical equivalent circuits [7] (Figure 2). The circuit I in Figure 2a illus-

trates the cell operation without parasitic currents through the membrane, resulting in a Faradaic efficiency close to 100%. In this scenario, no current flows through the cell when the applied voltage is below the thermo-neutral voltage (V_{tn}). Once the applied voltage surpasses V_{tn}, the total current ($i_t = i_{Faradaic}$) begins to flow through the cell, and the current–voltage relationship follows the typical polarization behaviour.

In the presence of parasitic currents through the membrane, circuit II in Figure 2b describes the behavior of the degraded cell. When the cell voltage is below V_{tn}, electronic current initially flows through short circuit paths in the membrane and is not used for water splitting, thus reducing hydrogen production. As the applied voltage increases, more current flows through these short circuit paths, collectively represented by R_{short} (comprising multiple resistors R_{s1}, R_{s2}, …, R_{sn} in parallel). Once the applied voltage exceeds V_{tn}, the water splitting starts, and part of the total current flows through proton transport within the membrane, leading to hydrogen generation. R_p represents the polarization resistance at the electrode/electrolyte interface and R_{el} accounts for the total Ohmic losses in the cell for both sets of data.

As opposed to the equivalent circuit representation above, we use as a basis the 1D physics-based model, which was implemented in our earlier work [40] and validated against experimental data [41], and adjusted it to account for short-circuit effects. This mathematical model was primarily built to support the multi-modal investigation of a new systematic aging phenomenon of current pathways which is caused by the cross-plane formation of iridium filaments within the membrane [34]. The latter study

a) Circuit I   b) Circuit II
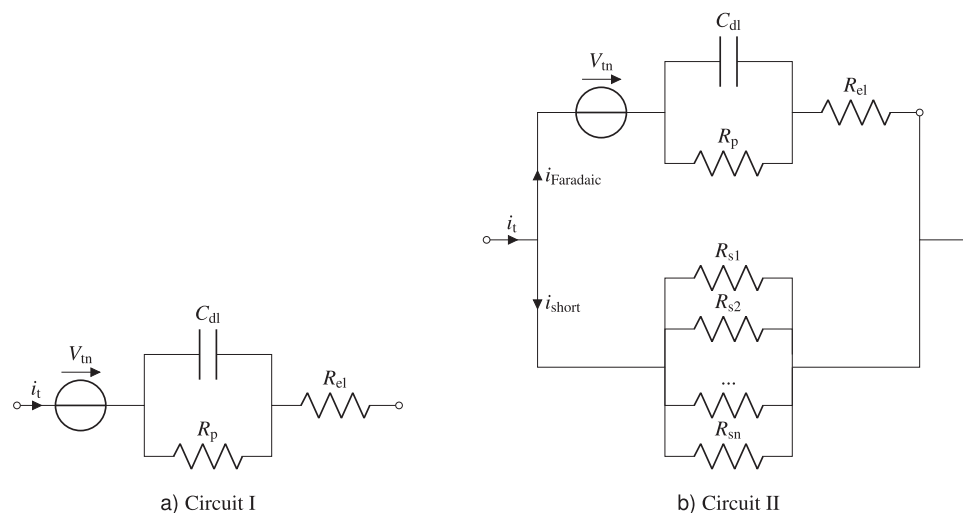
FIGURE 2 | Equivalent circuit representation of a healthy cell (a) and a degraded one exhibiting parasitic currents through MEA (b).
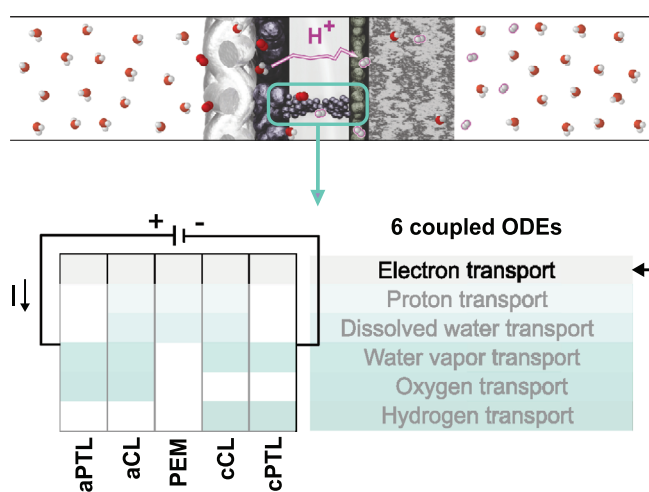
FIGURE 3 | Schematic overview of a five-layer PEMEC: Computational domain and equations included in the model.

reported that post-operated MEAs exhibited higher parasitic currents than the pristine ones.

Figure 3 shows a schematic overview of the computation domain of a five-layer PEMEC and how an electron-conductive pathway within PEM could look like in two dimensions. As already mentioned above, the model is one-dimensional and accounts for phenomena across the thickness of different layers. Therefore, it should be treated as a homogenized approach, which aims to show the cumulative effects of these electron-conductive pathways. In addition, we do not take into account any reactions that might occur on the surface of these pathways. We assume that there is no interaction between the electron transport in these pathways and the proton one in PEM. The model intends to give a macroscopic overview of short-circuit effects on the polarization behavior of PEMECs while assuming stationary and isothermal transport processes in the porous transport layers (PTLs), catalyst layers (CLs), and PEM [18, 42]. Oxygen and hydrogen are produced due to the oxygen and hydrogen evolution reaction (OER and HER), respectively. They behave as ideal gases and do not permeate the PEM. The reactions respect Butler–Volmer kinetics. The material components of MEA are supposed to be macroscopically homogeneous. The 1D five-layer MEA model can be described by six in total ordinary differential equations (ODEs), as summarized in Tables 1 and 2.

From Figure 3, it is clear that different transport mechanisms dominate in various components of the domain, and discontinuities are also present. Therefore, appropriate boundary conditions (BCs) must be defined for each neighboring component and second-order ODE These BCs are listed in Table 3. As previously mentioned, the membrane is impermeable to all gas species and water vapor. Consequently, the normal fluxes of gas species and water vapor are zero at the interface between PEM, aCL, and cathodic catalyst layer (cCL). Protons and dissolved water content are transported only in the ionomer phase, resulting in zero-flux BCs at the interfaces between CLs and PTLs. For the electrostatic potential, it is set to zero at the outer boundary of the cathodic porous transport layer (cPTL), while either a constant voltage or current can be applied to the aPTL boundary, as detailed in Table 3. Continuity is assumed at the remaining inner interfaces. In this model, there are pathways within PEM, which are electron conductive. Thus, electron transport in PEM is allowed and illustrated in Figure 4.

In Figure 4, the local potential distribution of electron (ϕ_e) and proton (ϕ_p) is presented. The BCs are also included in this schematic overview. In the catalyst layers, the OER and HER occur, resulting in the production and consumption of protons and electrons, respectively. The two equations describing the potential distribution have already been given in Table 1 (first two rows). The same holds for the source terms and BCs. Further details about the mathematical model, the parameters used in this study unless they are given again in the following sections, the computation model, and the UQ and SA framework can be found in our earlier publication [40]. All studies in Section 4 have been computed in galvanostatic mode.

Finally, we define Faradaic efficiency [18] since it will be utilized in our later studies to illustrate better the impact of parasitic

TABLE 1 | Governing equations.

Name	Unknown variable	Flux	Continuity equation	
Ohm's law for electrons	ϕ_e	$j_e = -\sigma_e^{eff} \nabla \phi_e$	$\nabla \cdot j_e = S_e$	(1)
Ohm's law for protons	ϕ_p	$j_p = -\sigma_p^{eff} \nabla \phi_p$	$\nabla \cdot j_p = S_p$	(2)
Water transport in ionomer	λ	$j_\lambda = -\frac{D_\lambda}{V_m} \nabla \lambda + \frac{\xi}{F} j_p$	$\nabla \cdot j_\lambda = S_\lambda$	(3)
Fick's law for water vapour	x_{H_2O}	$j_{H_2O} = -CD_{H_2O} \nabla x_{H_2O}$	$\nabla \cdot j_{H_2O} = S_{H_2O}$	(4)
Fick's law for oxygen	x_{O_2}	$j_{O_2} = -CD_{O_2} \nabla x_{O_2}$	$\nabla \cdot j_{O_2} = S_{O_2}$	(5)
Fick's law for hydrogen	x_{H_2}	$j_{H_2} = -CD_{H_2} \nabla x_{H_2}$	$\nabla \cdot j_{H_2} = S_{H_2}$	(6)

TABLE 2 | Source terms.

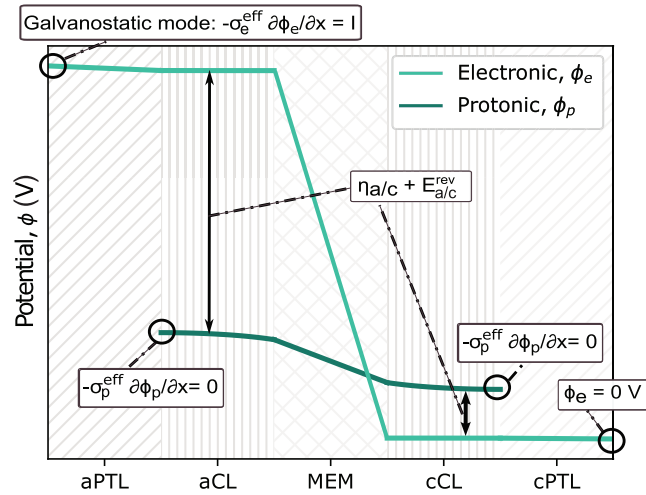| Source	aPTL	aCL	PEM	cCL	cPTL
S_e	0	$-R_a$	0	R_c	0
S_p	—	R_a	0	$-R_c$	—
S_λ	—	$S_{ad} - S_F$	0	S_{ad}	—
S_{H_2O}	0	$-S_{ad}$	—	$-S_{ad}$	0
S_{O_2}	0	$S_F/2$	—	—	—
S_{H_2}	—	—	—	S_F	0

FIGURE 4 | Schematic overview of local electron- and proton-potential distribution within the five layers of the computational domain.

currents on PEMECs. The Faradaic efficiency of H_2 can be represented by the following equation:

$$\eta_{H_2} = \frac{N_{H_2}^{cathode\ outlet}}{N_{H_2}^{theoretical}} = 1 - \frac{N_{H_2}^{crossover} + N_{H_2}^{recombination} + \frac{i_{short}}{2F}}{\frac{I}{2F}}, \quad (1)$$

where $N_{H_2}^{cathode\ outlet}$ is the molar flux of hydrogen at the cathode outlet, divided by the theoretical molar flux, $N_{H_2}^{theoretical}$, which is calculated using Faraday's law. The actual flux of hydrogen is lower than the theoretical flux, resulting in a Faraday efficiency below 100%, due to factors such as (i) electrical short currents, like those through the membrane [7], (ii) hydrogen losses from leaks and crossover through the membrane [28] and (iii) unwanted

side reactions, such as hydrogen recombining with permeated oxygen to form water at the cathode. In this work, the fluxes due to crossover and recombination are neglected since we do not account for these phenomena at the moment.

3 | Surrogate Model Development

The physics-based numerical model discussed in Section 2 involves the computation of six coupled non-linear partial differential equations. While the intrinsic complexity of solving such a system of equations leads to a better understanding of the physics and mechanistic details of the PEMEC, these models tend to be computationally expensive when we need to evaluate them repeatedly. Such a situation would arise when we want to optimize the system to find the best set of parameters for electrolyzer performance and perform UQ and SA for the entire system. In these circumstances, one may leverage surrogate models, primarily used to reduce computational effort. Surrogate models are simplified versions of the original model, developed by establishing a relationship between the input and output variables of the system. One of the ways to formulate this relationship is by the usage of data-driven models. Data-driven models are developed by learning the patterns in data and formulating relationships between input and output variables.

We develop data-based surrogate models in this work to perform UQ and SA. An XGBoost ML algorithm is deployed to develop these models since it offers a higher degree of explainability when compared to artificial neural networks [43]. The model is an ensemble method that uses a series of sequentially generated decision trees to make output predictions. The model begins by fitting weak learners to the negative gradient of the loss function and develops subsequent trees based on the residuals of the previous tree. Mathematically, it optimizes the following objective function for a given dataset $(x_i, y_i)_{i=1}^n$:

$$\text{Obj} = \sum_{i=1}^n L(y_i, \hat{y}_i) + \sum_{k=1}^K \Omega(f_k), \quad (2)$$

where the loss function $L(y_i, \hat{y}_i)$ is a squared loss function expressed by

$$L(y_i, \hat{y}_i) = (y_i - \hat{y}_1)^2 \quad (3)$$

and $\Omega(f_k)$ is the regularization term for the kth tree. The model's prediction is made by an additive combination of the output of all

TABLE 3 | Boundary conditions.

Variable	aCH/aPTL	aPTL/aCL	aCL/PEM	PEM /cCL	cCL/cPTL	cPTL/cCH
ϕ_e	Potentiostatic mode: $\phi_e = U$ Galvanostatic mode: $\sigma_e^{eff} \nabla \phi_e = I$	Continuity	Continuity	Continuity	Continuity	$\phi_e = 0$
ϕ_p	—	$n \cdot j_p = 0$	Continuity	Continuity	$n \cdot j_p = 0$	—
λ	—	$n \cdot j_\lambda = 0$	Continuity	Continuity	$n \cdot j_\lambda = 0$	—
x_{H_2O}	$x_{H_2O} = x_{H_2O}^a$	Continuity	$n \cdot j_{H_2O} = 0$	$n \cdot j_{H_2O} = 0$	Continuity	$x_{H_2O} = x_{H_2O}^c$
x_{O_2}	$x_{O_2} = x_{O_2}^a$	Continuity	$n \cdot j_{O_2} = 0$	—	—	—
x_{H_2}	—	—	—	$n \cdot j_{H_2} = 0$	Continuity	$x_{H_2} = x_{H_2}^c$

TABLE 4 | Range of the input parameters considered to build the data-driven surrogate models.

Input (Feature vectors)	Unit	Range of values
$\epsilon_{m,aCL}$	—	$0.3 - 0.7$
$\epsilon_{m,cCL}$	—	$0.3 - 0.7$
l_{aCL}	μm	$6 - 18$
l_{pem}	μm	$90 - 180$
l_{cCL}	μm	$6 - 18$
$\sigma_{e,aCL}^{eff}$	$S\,m^{-1}$	$0.035 - 350$
$\sigma_{e,pem}^{eff}$	$S\,m^{-1}$	$10^{-4} - 10^{-1}$
$\sigma_{e,cCL}^{eff}$	$S\,m^{-1}$	$0.035 - 350$

the trees

$$\hat{y}_i = \sum_{k=1}^{K} f_k(x_i). \tag{4}$$

The data to train the model were generated from the 1D physics-based model by varying a range of parameters enlisted in Table 4. Since our focus in this study is on short-circuit effects, we have limited our attention to the geometric and electron transport properties of catalysts and the membrane. A database consisting of 945,667 data points was generated with the electrolyzer being operated galvanostatically for current densities, ranging from 0.1 up to 2 Acm^{-2}. The hyperparameters of the ML surrogate model were set as follows: learning rate = 0.015, maximum tree depth = 6, and number of estimators = 700.

4 | Results

We begin our discussions by first performing a one-at-a-time parameter study to understand the impact of electronic pathways within PEM on cell performance and Faradaic efficiency. Afterwards, we explore the possibility of generation of surrogate models through machine-learning algorithms. These surrogate models are robust and ideal for stochastic modeling and our later UQ and SA studies.

### 4.1 | One-at-a-Time Parameter Study

The deterministic physics-based model gives a detailed insight into the dependence of the polarization behavior on the electronic

conductivity of possible electron-conductive pathways within PEM. The parametric study in Figure 5 is performed to determine their interplay. On the left side of the figure, the short-circuit influence on the polarization behavior is shown, whereas its impact on the Faradaic efficiency of hydrogen is presented on the right side. A huge impact on the polarization curve is observed when the electronic conductivity of the electronic pathways gets higher than $10^{-2} \frac{S}{m}$. Current flows through the cell even for voltages below open circuit voltage. This is also in qualitative agreement with the polarization behavior of pristine and post-operated MEAs, presented in a recent multi-modal analysis of cross-plane iridium-based filaments [34]. A decrease in the Faradaic efficiency of hydrogen is also computationally estimated, as expected, and reported in the literature [27, 29]. In Figure 6a, we plot the through-plane potential distribution for all layers. Since the differences were not visible enough, we also present the through-plane potential profile for the anode side (aPTL, aCL), the PEM, and the cathode side (cPTL, cCL) separately (Figure 6b–d). Similarly, we plot the distribution of current density in Figure 6f–h). The influence of the electron-conductive pathways within PEM becomes evident when the effective conductivity increases. From Figure 6g, we realize that not all the current density is employed for water splitting, thus decreasing the efficiency of our system accordingly.

4.2 | Data-Driven Model Performance

From the preceding section, we observe that quantitative and qualitative insights can be obtained from the 1D PEMEC model by performing a one-at-a-time parametric study. However, if we aim to conduct an SA or UQ, we must repeat thousands of computations. This becomes computationally expensive even for a 1D model, especially when we are exploring a wide parameter space with a large number of computations. To accomplish SA and UQ, we have developed a data-driven surrogate model as described in Section 3. We now look into the performance of the developed model.

To develop the model, we initially split the entire data into training and testing datasets. This division was done using a split ratio of 80:20 to randomly divide the data. The training dataset is used to develop the model, whereas the test dataset is used to calibrate the model's performance. Figure 7a,b shows the relationship between the predicted voltage and ground truth for the training and testing datasets, respectively. We notice a good fit between the model's prediction and the actual data
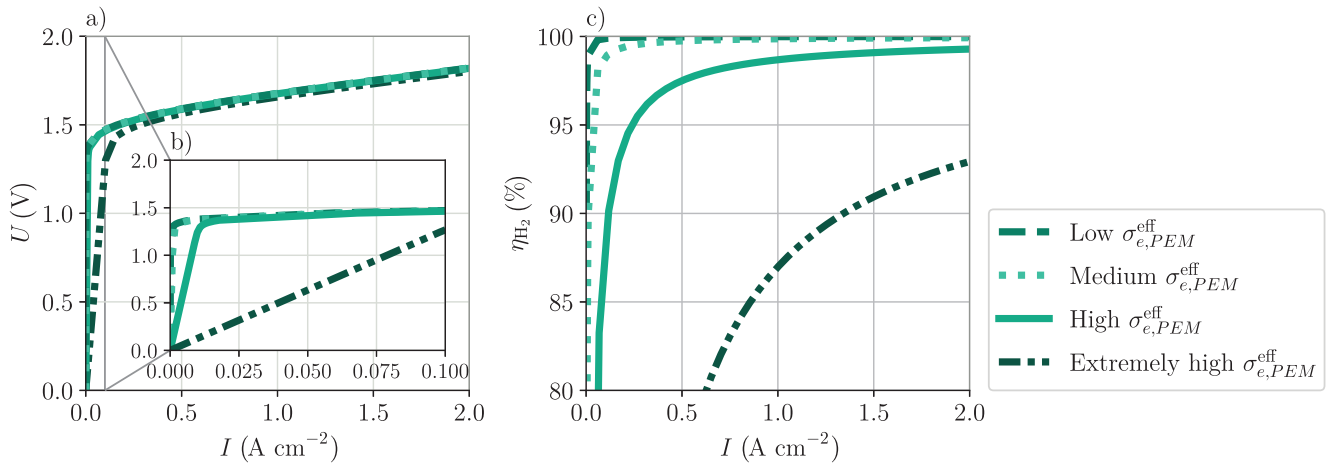
FIGURE 5 | Parameter study for the influence of electronic pathways within PEM on the cell polarization behavior (a) and Faradaic efficiency (c). The effect on the polarization curve is more evident when we zoom in at lower current densities (b). The higher the electronic conductivity is, the less efficient PEMECs are. The low $\sigma_{e,PEM}^{\mathrm{eff}}$ corresponds to a value of 10^{-4} Sm^{-1}, the medium one to 10^{-3} Sm^{-1}, the high one to 10^{-2} Sm^{-1} and the extremely high one to 10^{-1} Sm^{-1}.

obtained from the 1D PEMEC model. To further quantify the model performance, we define the mean square error (MSE) and the coefficient of determination (R^2) mathematically, as expressed below:

$$\mathrm{MSE} = \frac{1}{n}\sum_{j=1}^{n}(y_j - \hat{y}_j)^2, \tag{5}$$

$$R^2 = 1 - \frac{\frac{1}{n}\sum_{j=1}^{n}(y_j - \hat{y}_j)^2}{\frac{1}{n}\sum_{i=1}^{n}(y_j - \bar{y}_j)^2}, \tag{6}$$

where n denotes the number of samples, y_j represents the ground truth obtained from the analytical model, $\hat{y}$ denotes the predicted values and $\bar{y}$ is the average value of y_j. The R^2 value for both the training and test dataset is greater than 0.99. This implies that there exists a strong correlation between the surrogate model's prediction and the actual values obtained from the physics-based numerical model. The MSE for the training and test data are 1.14×10^{-4} and 1.23×10^{-5}, respectively. Apart from voltage predictions, we trained the data-driven surrogate model to predict the Faradaic efficiency, as illustrated in Figure 7c,d). The same set of split ratio and hyperparameters was used to develop this model. With the R^2 values greater than 0.999 and MSE lesser than 10^{-6}, the model shows good predictive performance for Faradaic efficiency on both training and test datasets.

To further evaluate the model's performance, we plot the polarization and efficiency curves and compare them with the corresponding curves generated from the 1D numerical model. To make this comparison, we take the following random conditions: $\epsilon_{m,aCL} = 0.5$, $\epsilon_{m,cCL} = 0.3$, $l_{aCL} = 6\,\mu m$, $l_{pem} = 90\,\mu m$, $l_{cCL} = 6\,\mu m$, $\sigma_{e,aCL}^{\mathrm{eff}} = 0.35\,\mathrm{Sm}^{-1}$ and $\sigma_{e,cCL}^{\mathrm{eff}} = 0.35\,\mathrm{Sm}^{-1}$. The two test cases differ in their values for the $\sigma_{e,pem}^{\mathrm{eff}}$, as shown in Figure 8a. It is to be noted that these data points were not a part of the original training and test datasets. We see from Figure 8a,b that the predictions from the surrogate model match well with those obtained by the numerical simulations. Both the values and the trends in the variation of voltage and Faradaic efficiency as a function of

current density as captured by the surrogate model. In particular, we notice for high $\sigma_{e,pem}^{\mathrm{eff}}$ the Faradaic efficiency shows a sharp increase as the current density is increased to $1.0\,\mathrm{Acm}^{-2}$. This rate of increment in Faradaic efficiency is then damped as the current density is further increased. The XGBoost model exhibits its accuracy in capturing this trend. Now that we have developed and calibrated the accuracy of the surrogate model, we deploy this for performing SA in the next section.

4.3 | Stochastic Approach and SA

We have conducted an SA study (Figures 9 and 10) to understand better the interplay between various input parameters (e.g., the ionomer volume fraction in CLs, the layer thicknesses of CLs and PEM, and the effective electric conductivity in CLs and PEM) and the model outputs, such as the polarization behavior and Faradaic efficiency of PEMECs. We assume that these input parameters behave as random variables and are independent of each other, and we assign them a uniform probability density function (PDF) as presented in Table 5. The upper and lower bounds of their assigned PDFs were chosen based on the references given in Table 5. The choice of a uniform PDF was based on other SA studies [44, 45], which assumed uniform PDFs for the uncertain input parameters. In the case of adequate experimental observations in a random sample, we can use these observations to estimate the PDFs using a histogram, which is a classical method of density estimation. However, enough observations were not available for this work, especially for the effective electric conductivities within the membrane. Therefore, we considered the uniform PDF a logical assumption for this initial study. In Figure 9, we present the first-order and total-order Sobol indices (SI) for the averaged potential.

At this point, we need to remind the readers of the difference between the first-order and total-order SIs. The total-order SI accounts for both the sensitivity from first-order effects and the sensitivity resulting from interactions between a specific parameter and all other parameters. The sum of the total-order
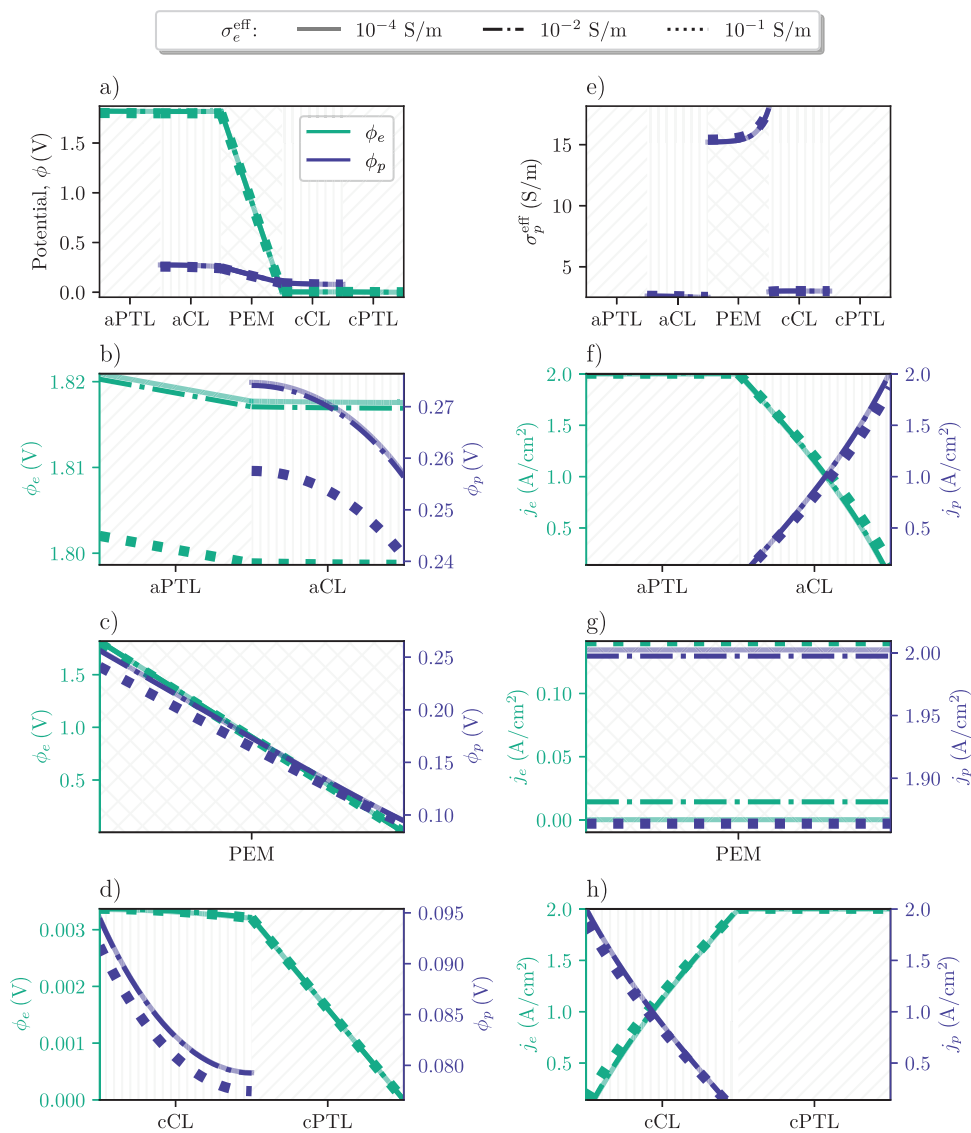
FIGURE 6 | Comparison of the through-plane potential profiles (a)–(d), the effective protonic conductivity, σ_p^{eff} (e) and the current density distributions (f)–(h) at $I = 2.0\,\text{Acm}^{-2}$ by assuming different effective electronic conductivity of the electron conductive pathways within PEM.

TABLE 5 | Uncertainty range and probability distribution functions of the input parameters, taken into account for the global SA.

| Parameter	Unit	Uncertainty Range	Distribution	Reference
$\epsilon_{\text{m,aCL}}$	—	$[0.3, 0.7]$	$\mathcal{U}(0.3, 0.7)$	[44]
$\epsilon_{\text{m,cCL}}$	—	$[0.3, 0.7]$	$\mathcal{U}(0.3, 0.7)$	[44]
l_{aCL}	µm	$[6, 18]$	$\mathcal{U}(6, 18)$	[44]
l_{pem}	µm	$[90, 180]$	$\mathcal{U}(90, 180)$	[42]
l_{cCL}	µm	$[6, 18]$	$\mathcal{U}(6, 18)$	[44]
$\sigma_{\text{e,aCL}}^{\text{eff}}$	S m^{-1}	$[0.035, 350]$	$\mathcal{U}(0.035, 350)$	[42]
$\sigma_{\text{e,pem}}^{\text{eff}}$	S m^{-1}	$[10^{-4}, 10^{-1}]$	$\mathcal{U}(10^{-4}, 10^{-1})$	[34]
$\sigma_{\text{e,cCL}}^{\text{eff}}$	S m^{-1}	$[0.035, 350]$	$\mathcal{U}(0.035, 350)$	[42]
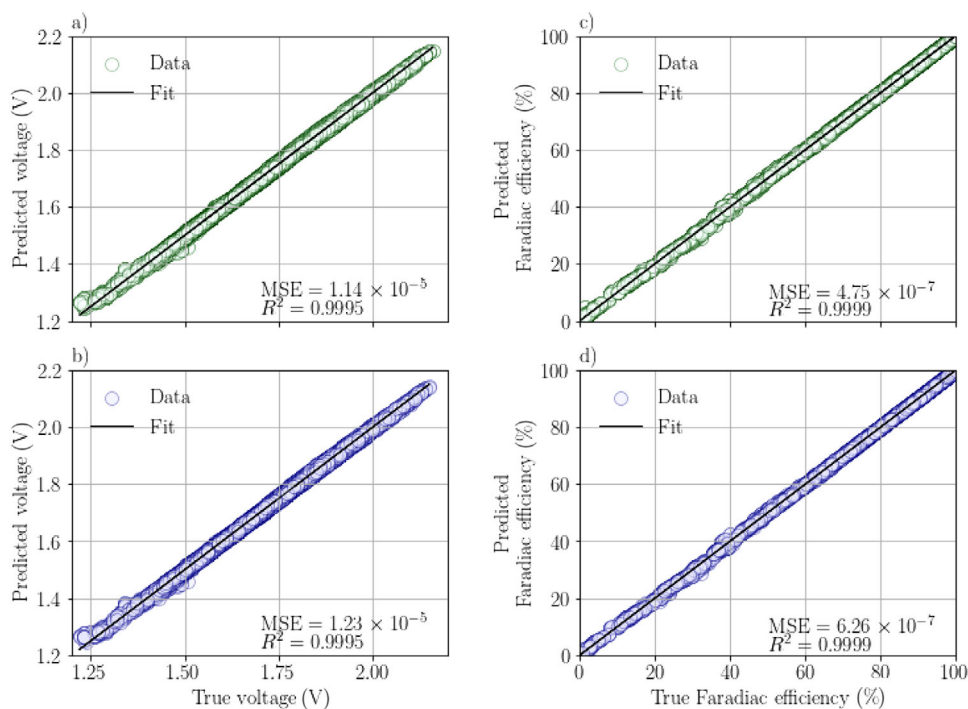
FIGURE 7 | Comparison between the predicted voltage and Faradiac efficiencies and those obtained from the 1D numerical model for the training (a,c) and test (b,d) datasets.
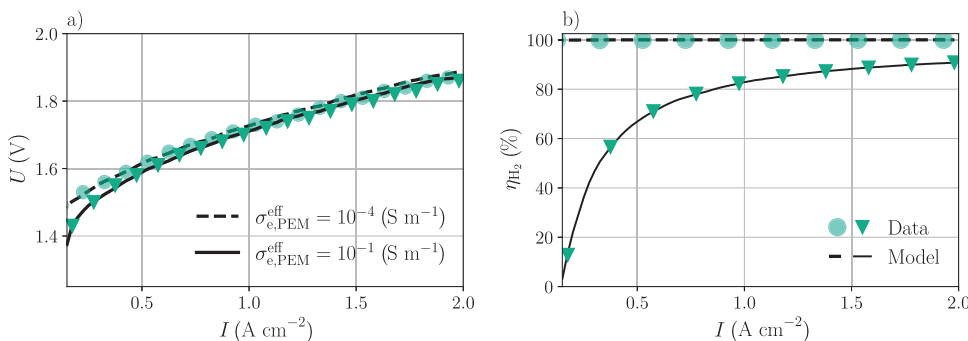
FIGURE 8 | Polarization curves (a) and Faradiac efficiencies (b) for two different effective electronic conductivities of the electron-conductive pathways within the membrane.
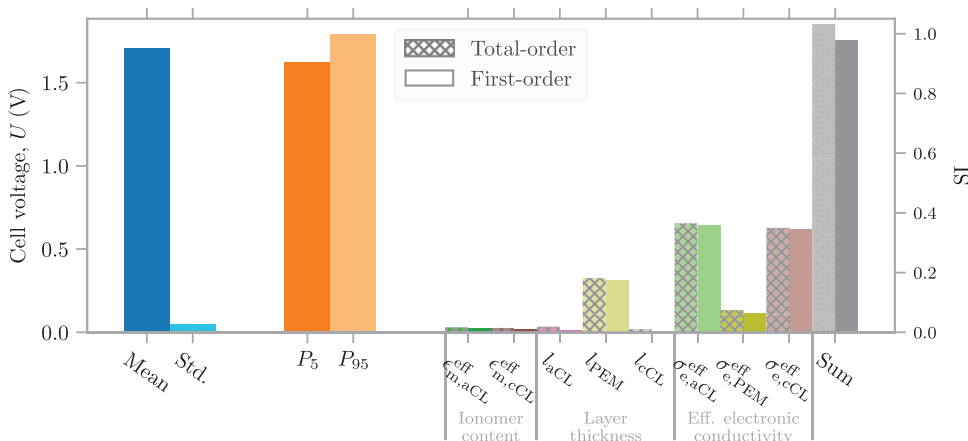
FIGURE 9 | The average cell potential as computed by means of the ML surrogate model. Mean, standard deviation (SD), and 90% PI are presented on the left side, whereas the total-order and first-order SI of the averaged cell potential over current density are presented on the right side. The 90% prediction interval (PI) is indicated by the 5th and 95th percentiles, that is, 90% of the cell potential is between P_5 and P_{95}.
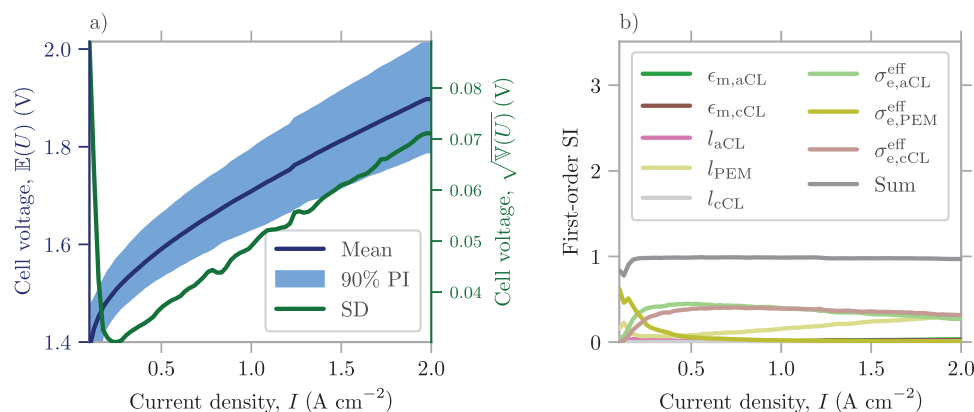
FIGURE 10 | UQ and SA for different features based on the ML surrogate model. The mean, SD, and 90% prediction interval (PI) of cell voltage over current density are presented on the left (Figure 9a), and the first-order SIs of cell voltage over current density on the right (Figure 9b).

SIs is equal to or greater than one. If no higher-order interactions exist, the sum of the first-order and total-order SIs will be equal to one. From Figure 9, we realize that there are slight differences between the first-order and total-order SIs, which are more evident in their sums. However, these differences are small, indicating that higher-order interactions are not crucial for the interplay between the polarization behavior and the considered input parameters.

From Figure 9, the most influential parameters for the polarization behavior are the effective electric conductivities and the PEM layer thickness. We expect that the effective electric conductivity of PEM due to the parasitic current pathways is crucial at very low current densities, as indicated in our earlier work [34] and confirmed by this analysis and the above parametric study (see Figures 5 and 8). Furthermore, the PEM thickness is of great significance as it was also commented on in our earlier study [40]. Another important finding of this analysis is that the impact of effective electric conductivity in CLs is high. For this study, we consider a broad uncertainty range for these two input parameters, covering the case for both unsupported and supported CLs [43]. Unfortunately, very low electric conductivities in CLs have a negative impact on cell performance.

In Figure 10, we show which input parameter is responsible for deviations from the mean polarization curve in the range of investigated current densities. As already described in the above one-at-a-time parameter study and Figure 5, the effective electric conductivity of PEM is mostly influential for very low current densities, lower than $0.5\,\mathrm{Acm^{-2}}$. This is also confirmed by SA in Figure 10. The PEM thickness influences the polarization behavior in the beginning (current densities below $0.25\,\mathrm{Acm^{-2}}$) and mostly for higher current densities than $1.0\,\mathrm{Acm^{-2}}$. In addition, the sum of first-order SIs is way lower than 1.0 for current densities below $0.25\,\mathrm{Acm^{-2}}$, which indicates an interaction between the thickness and effective electric conductivity of PEM.

5 | Conclusions

In this work, we presented a 1D mathematical model that describes the parasitic current effects besides the main transport

phenomena occurring in a five-layer PEMEC. The implementation was fully done in Python and based on the SOLVE_BVP solver from the submodule SCIPY.INTEGRATE, as in our earlier work [40]. The parasitic current effects in PEMECs are further assessed using an ML technique, namely XGBoost. Training data for these algorithms is derived from a 1D physics-based model of PEMEC. Input features primarily include parameters related to the material design of the MEA. Statistical error metrics, such as the MSE, and R^2 are employed to evaluate and compare the predictive accuracy of the surrogate model on both training and test datasets. For further analysis and with this surrogate model as a basis, we employed our already developed framework for UQ and global SA based on the libraries CHAOSPY [46] and UNCERTAINPY [47] to study the interplay between input parameters and model output.

Regarding the key findings of this work, the one-at-a-time parameter study revealed that possible electron-conductive pathways within PEM have an essential impact on cell performance and Faradaic efficiency. The higher their effective electronic conductivity is, the less efficient PEMECs are. Additionally, in our SA studies, we confirmed that the effective electric conductivity of PEM is mostly influential for very low current densities. The most influential parameters for the polarization behavior are the effective electric conductivity of PEM and CLs and the PEM layer thickness.

Finally, it is important to acknowledge a certain limitation associated with solely using synthetic data derived from physics-based simulations to train ML surrogate models. Physical models are often an idealized representation of real applications. Therefore, an ML surrogate model, purely trained on synthetic data, can only replicate the predictive accuracy of the used physical models, which might fail to generalize real-world conditions. To address this limitation, we plan to improve the accuracy of trained surrogate models by employing experimental observations from cell experiments to train and test ML models. Moreover, due to the complexity of the real-world applications, a model and its SA results require extensive amounts of high-quality experimental data, which can become available nowadays employing high-throughput experimentation (HTE) [48]. We intend to take advantage of the available HTE facilities to validate the presented model in this work, and our simulations in general.

List of Symbols

Sign	Description	Unit	Page list
D_λ	water diffusivity in the ionomer phase	m^2s^{-1}	5
V_m	molar volume of dry electrolyte per SO_3^- group	m^3mol^{-1}	5
$\varepsilon_{m,aCL}$	ionomer volume fraction in aCL	—	7
$\varepsilon_{m,cCL}$	ionomer volume fraction in cCL	—	7
λ	water content in the ionomer phase	—	5
F	Faraday constant	$C\,mol^{-1}$	5
ϕ_e	electronic potential	V	5
ϕ_p	protonic potential	V	5
σ_p^{eff}	effective proton conductivity	$S\,m^{-1}$	5
$\sigma_{e,aCL}^{eff}$	effective electron conductivity in aCL	$S\,m^{-1}$	7
$\sigma_{e,cCL}^{eff}$	effective electron conductivity in cCL	$S\,m^{-1}$	7
$\sigma_{e,pem}^{eff}$	effective electron conductivity in PEM	$S\,m^{-1}$	7
σ_e^{eff}	effective electron conductivity	$S\,m^{-1}$	5
ξ	electro-osmotic drag (EOD) coefficient	—	5
l_{aCL}	aCL layer thickness	m	7
l_{cCL}	cCL layer thickness	m	7
l_{pem}	PEM layer thickness	m	7
x_{H_2O}	molar fraction of water vapour	—	5
x_{H_2}	molar fraction of hydrogen	—	5
x_{O_2}	molar fraction of oxygen	—	5

Author Contributions

Violeta Karyofylli: writing–original draft, visualization, validation, software, methodology, investigation, conceptualization. **K. Ashoke Raman:** writing–original draft, visualization, validation, software, methodology, investigation. **Linus Hammacher:** writing–original draft, software, methodology, investigation.**Yannik Danner:** Writing–original draft, investigation. **Hans Kungl:** writing–review & editing, supervision, project administration, funding acquisition. **André Karl:** writing–review & editing, project administration. **Eva Jodat:** writing–review & editing, project administration. **Rüdiger-A. Eichel** Writing–review & editing, supervision, project administration, funding acquisition.

Conflicts of Interest

The authors declare no conflicts of interest.

Data Availability Statement

Data will be made available on request.

References

1. DECHEMA, acatech(ed.) *Comparative Analysis of International Hydrogen Strategies*, Country Analysis 2023. Technical report (DECHEMA, acatech, 2024).

2. Bundesministerium für Wirtschaft und Energie, "Nationale Wasserstoffstrategie," Technical Report (BMWi, 2020).

3. Bundesministerium für Wirtschaft und Klimaschutz, "Fortschreibung Der Nationalen Wasserstoffstrategie," Technical Report (BMWK, 2023).

4. H. Marefatjouikilevaee, F. Auger, and J. C. Olivier, "Static and Dynamic Electrical Models of Proton Exchange Membrane Electrolysers: A Comprehensive Review," *Energies* 16, no. 18 (2023): 6503.

5. D. Guilbert and G. Vitale, "Hydrogen as a Clean and Sustainable Energy Vector for Global Transition from Fossil-Based to Zero-Carbon," *Clean Technologies* 3, no. 4 (2021): 881–909.

6. N. Norazahar, F. Khan, N. Rahmani, and A. Ahmad, "Degradation Modelling and Reliability Analysis of PEM Electrolyzer," *International Journal of Hydrogen Energy* 50 (2024): 842–856.

7. S. P. S. Badwal, S. Giddey, and F. T. Ciacchi, "Hydrogen and Oxygen Generation With Polymer Electrolyte Membrane (PEM)-Based Electrolytic Technology," *Ionics* 12, no. 1 (2006): 7–14.

8. M. Carmo, D. L. Fritz, J. Mergel, and D. Stolten, "A Comprehensive Review on PEM Water Electrolysis," *International Journal of Hydrogen Energy* 38, no. 12 (2013): 4901–4934.

9. S. Siracusano, N. Van Dijk, R. Backhouse, L. Merlo, V. Baglio, and A. Aricò, "Degradation Issues of PEM Electrolysis MEAs," *Renewable Energy* 123 (2018): 52–57.

10. U. Babic, M. Suermann, F. N. Büchi, L. Gubler, and T. J. Schmidt, "Critical Review'Identifying Critical Gaps for Polymer Electrolyte Water Electrolysis Development," *Journal of The Electrochemical Society* 164, no. 4 (2017): F387–F399.

11. U. Babic, M. Tarik, T. J. Schmidt, and L. Gubler, "Understanding the Effects of Material Properties and Operating Conditions on Component Aging in Polymer Electrolyte Water Electrolyzers," *Journal of Power Sources* 451 (2020): 227778.

12. P. Millet, A. Ranjbari, F. De Guglielmo, S. Grigoriev, and F. Auprêtre, "Cell Failure Mechanisms in PEM Water Electrolyzers," *International Journal of Hydrogen Energy* 37, no. 22 (2012): 17478–17487.

13. A. Kalinnikov, S. Grigoriev, and D. Bessarabov, "Numerical Analysis of the Electrochemical Dissolution of Iridium Catalyst and Evaluation of Its Effect on the Performance of Polymer Electrolyte Membrane Water Electrolyzers," *International Journal of Hydrogen Energy* 48, no. 59 (2023): 22342–22365.

14. Q. Feng, X. Yuan, G. Liu, et al., "A Review of Proton Exchange Membrane Water Electrolysis on Degradation Mechanisms and Mitigation Strategies," *Journal of Power Sources* 366 (2017): 33–55.

15. S. Grigoriev, K. Dzhus, D. Bessarabov, and P. Millet, "Failure of PEM Water Electrolysis Cells: Case Study Involving Anode Dissolution and Membrane Thinning," *International Journal of Hydrogen Energy* 39, no. 35 (2014): 20440–20446.

16. E. Kuhnert, M. Heidinger, D. Sandu, V. Hacker, and M. Bodner, "Analysis of PEM Water Electrolyzer Failure Due to Induced Hydrogen

Crossover in Catalyst-Coated PFSA Membranes," *Membranes* 13, no. 3 (2023): 348.

17. L. Placca and R. Kouta, "Fault Tree Analysis for PEM Fuel Cell Degradation Process Modelling," *International Journal of Hydrogen Energy* 36, no. 19 (2011): 12393–12405.

18. P. Trinke, "Experimental and Model-Based Investigations on Gas Crossover in Polymer Electrolyte Membrane Water Electrolyzers," (PhD thesis., ottfried Wilhelm Leibniz Universität, 2021).

19. T. Franz, G. Papakonstantinou, and K. Sundmacher, "Transient Hydrogen Crossover in Dynamically Operated PEM Water Electrolysis Cells - A Model-Based Analysis," *Journal of Power Sources* 559 (2023): 232582.

20. S. H. Frensch, F. Fouda-Onana, G. Serre, D. Thoby, S. S. Araya, and S. K. Kær, "Influence of the Operation Mode on PEM Water Electrolysis Degradation," *International Journal of Hydrogen Energy* 44, no. 57 (2019): 29889–29898.

21. N. Li, S. S. Araya, and S. K. Kær, "The Effect of Fe^{3+} Contamination in Feed Water on Proton Exchange Membrane Electrolyzer Performance," *International Journal of Hydrogen Energy* 44, no. 26 (2019): 12952–12957.

22. N. Li, S. S. Araya, and S. K. Kær, "Long-Term Contamination Effect of Iron Ions on Cell Performance Degradation of Proton Exchange Membrane Water Electrolyser," *Journal of Power Sources* 434 (2019): 226755.

23. T. Sugawara, N. Kawashima, and T. N. Murakami, "Kinetic Study of Nafion Degradation by Fenton Reaction," *Journal of Power Sources* 196, no. 5 (2011): 2615–2620.

24. M. Chandesris, V. Médeau, N. Guillet, S. Chelghoum, D. Thoby, and F. Fouda-Onana, "Membrane Degradation in PEM Water Electrolyzer: Numerical Modeling and Experimental Evidence of the Influence of Temperature and Current Density," *International Journal of Hydrogen Energy* 40, no. 3 (2015): 1353–1366.

25. C. C. Weber, J. A. Wrubel, L. Gubler, G. Bender, S. De Angelis, and F. N. Büchi, "How the Porous Transport Layer Interface Affects Catalyst Utilization and Performance in Polymer Electrolyte Water Electrolysis," *ACS Applied Materials & Interfaces* 15, no. 29 (2023): 34750–34763.

26. C. Liu, J. Wrubel, E. Padgett, and G. Bender, "The Impacts of Membrane Pinholes on PEM Water Electrolysis," *Journal of Power Sources* 581 (2023): 233507.

27. T. T. Phan, S. K. Kim, J. Islam, M. J. Kim, and J. H. Lee, "Degradation Analysis of Polymer Electrolyte Membrane Water Electrolyzer With Different Membrane Thicknesses," *International Journal of Hydrogen Energy* 49 (2024): 875–885.

28. G. De Moor, N. Charvin, C. Bas, N. Caque, E. Rossinot, and L. Flandin, "In Situ Quantification of Electronic Short Circuits in PEM Fuel Cell Stacks," *IEEE Transactions on Industrial Electronics* 62, no. 8 (2015): 5275–5282.

29. C. Klose, T. Saatkamp, A. Münchinger, et al., "All-Hydrocarbon MEA for PEM Water Electrolysis Combining Low Hydrogen Crossover and High Efficiency," *Advanced Energy Materials* 10, no. 14 (2020): 1903995.

30. S. S. Kocha, J. D. Yang, and J. S. Yi, "Characterization of Gas Crossover and Its Implications in PEM Fuel Cells," *AIChE Journal* 52, no. 5 (2006): 1916–1925.

31. F. Grumm, M. Schumann, C. Cosse, M. Plenz, A. Lücken, and D. Schulz, "Short Circuit Characteristics of PEM Fuel Cells for Grid Integration Applications," *Electronics* 9, no. 4 (2020): 602.

32. H. Xu, B. Rasimick, M. Riera-Smith, et al., "High-Performance, Long-Lifetime Catalysts for Proton Exchange Membrane Electrolysis Final Report Period Covering April 22, 2013 to April 21, 2015." (2015).

33. Z. Zeng, R. Ouimet, L. Bonville, et al., "Degradation Mechanisms in Advanced MEAs for PEM Water Electrolyzers Fabricated by Reactive Spray Deposition Technology," *Journal of The Electrochemical Society* 169, no. 5 (2022): 054536.

34. C. Heume, V. Karyofylli, A. Javed, et al., "Cross-Plane Iridium-Based Filaments Sap Efficiency in Proton Exchange Membrane Electrolyzers," Preprint (Version 1), Research Square, October 28, https://doi.org/10.21203/rs.3.rs-5337119/v1.

35. P. Olivier, C. Bourasseau, and P. B. Bouamama, "Low-Temperature Electrolysis System Modelling: A Review," *Renewable and Sustainable Energy Reviews* 78 (2017): 280–300.

36. S. A. Grigoriev, A. A. Kalinnikov, P. Millet, V. I. Porembsky, and V. N. Fateev, "Mathematical Modeling of High-Pressure PEM Water Electrolysis," *Journal of Applied Electrochemistry* 40, no. 5 (2010): 921–932.

37. E. Crespi, G. Guandalini, L. Mastropasqua, S. Campanari, and J. Brouwer, "Experimental and Theoretical Evaluation of a 60 kW PEM Electrolysis System for Flexible Dynamic Operation," *Energy Conversion and Management* 277 (2023): 116622.

38. J. Giner-Sanz, E. Ortega, and V. Pérez-Herranz, "Hydrogen Crossover and Internal Short-Circuit Currents Experimental Characterization and Modelling in a Proton Exchange Membrane Fuel Cell," *International Journal of Hydrogen Energy* 39, no. 25 (2014): 13206–13216.

39. C. Yuhn, M. Oshima, Y. Chen, M. Hayakawa, and S. Yamada, "Uncertainty Quantification in Cerebral Circulation Simulations Focusing on the Collateral Flow: Surrogate Model Approach With Machine Learning," *PLoS Computational Biology* 18, no. 7 (2022): e1009996.

40. V. Karyofylli, Y. Danner, K. A. Raman, et al., "Sensitivity Analysis and Uncertainty Quantification in Predictive Modeling of Proton-Exchange Membrane Electrolytic Cells," *Journal of Power Sources* 600 (2024): 234209.

41. M. Chandesris, V. Médeau, N. Guillet, S. Chelghoum, D. Thoby, and F. Fouda-Onana, "Membrane Degradation in PEM Water Electrolyzer: Numerical Modeling and Experimental Evidence of the Influence of Temperature and Current Density," *International Journal of Hydrogen Energy* 40, no. 3 (2015): 1353–1366.

42. P. A. García-Salaberri, "1D Two-Phase, Non-Isothermal Modeling of a Proton Exchange Membrane Water Electrolyzer: An Optimization Perspective," *Journal of Power Sources* 521 (2022): 230915.

43. K. A. Raman, L. Hammacher, H. Kungl, et al., "Data-Driven Surrogate Modeling for Performance Prediction and Sensitivity Analysis of Transport Properties in Proton Exchange Membrane Water Electrolyzer," *Applied Energy*, 386 (2025), 125529.

44. R. Vetter and J. O. Schumacher, "Experimental Parameter Uncertainty in Proton Exchange Membrane Fuel Cell Modeling. Part II: Sensitivity Analysis and Importance Ranking," *Journal of Power Sources* 439 (2019): 126529.

45. L. M. Pant, S. Stewart, N. Craig, and A. Z. Weber, "Critical Parameter Identification of Fuel-Cell Models Using Sensitivity Analysis," *Journal of The Electrochemical Society* 168, no. 7 (2021).

46. J. Feinberg and H. P. Langtangen, "Chaospy: An Open Source Tool for Designing Methods of Uncertainty Quantification," *Journal of Computational Science* 11 (2015): 46–57.

47. S. Tennøe, G. Halnes, and G. T. Einevoll, "Uncertainpy: A Python Toolbox for Uncertainty Quantification and Sensitivity Analysis in Computational Neuroscience," *Frontiers in Neuroinformatics* 12 (2018): 49.

48. D. Dogan, B. Hecker, X. Hou, et al., "A Well-Advanced High-Throughput Test System for Electrocatalytic Screening Applications Under Industrial Relevant Conditions – A Perspective to Accelerate Electrolysis Research and Development," *Electrochemical Science Advances*, ahead of print, November 3, 2024, https://doi.org/10.1002/elsa.202400015.

49. Jülich Supercomputing Centre, "JURECA: Data Centric and Booster Modules implementing the Modular Supercomputing Architecture at Jülich Supercomputing Centre," *Journal of Large-Scale Research Facilities* 7, no. A182 (2021).